ECCOMAS Congress 2016
VII European Congress on Computational Methods in Applied Sciences and Engineering
M. Papadrakakis, V. Papadopoulos, G. Stefanou, V. Plevris (eds.)
Crete Island, Greece, 5–10 June 2016

A MESHLESS METHOD FOR SIMULATION OF PARTICLE-DRIVEN GRAVITY CURRENTS WITH OBSTACLES

Karel Kovářík[1], **Juraj Mužík**[1], **and Dana Sitányiová**[1]

[1]University of Žilina, Department of Geotechnics
Univerzitna 8215/1 Žilina, Slovakia
e-mail: karel.kovarik, juraj.muzik, dana.sitanyiova@fstav.uniza.sk

Keywords: gravity current, LBIEM, obstacle, meshless method

Abstract. *A meshless local boundary integral equation method (LBIEM) is used to analyse gravity currents flow in two-dimensional domains. The method solves the incompressible Navier–Stokes equations with a transport equation for the particle concentration. The characteristic-based split scheme is used to solve the governing equations. The LBIEM basic equations are derived via interpolation using radial basis functions. Numerical test cases of the lock-exchange channel flow with obstacles in its bed are presented here.*

1 INTRODUCTION

Gravity currents increase when a heavier fluid propagates into a lighter one. This phenomena is frequently encountered in environment applications and geohazards (like solifluction, debris flow or turbidity currents). Particle-driven gravity currents create a special group of these flows when the difference in density is caused by the concentration of suspended particles. The particles may settle or become resuspended. For this reason these currents are known as non-conservative gravity currents [1]. Moreover, particles do not exactly follow the fluid flow. When the size of particles is small the velocity of particles can be expressed as a sum of the fluid velocity and a constant settling velocity [2].

2 GOVERNING EQUATIONS

The motion of the fluid phase is governed by the Navier-Stokes equations which can be written in its primitive variables as

$$\frac{\partial u_i}{\partial x_i} = 0 \tag{1}$$

$$\frac{\partial u_i}{\partial t} + \frac{\partial}{\partial x_j}\left(u_j u_i\right) = \nu \frac{\partial^2 u_i}{\partial x_j \partial x_j} - \frac{1}{\rho}\frac{\partial p}{\partial x_i} - \frac{C}{\rho} F_i$$

where u_i is the fluid velocity vector component, *p* is the pressure, ν is the kinematic viscosity, ρ is the density of a liquid, *C* is the particle-number density (i.e. the concentration), and F_i represents Stoke's drag which is the dominant flow force on an individual particle in direction *i* [3]. The particle field can be treated in an Eulerian manner (see [3]) and is governed by the following advection-diffusion equation

$$\frac{\partial C}{\partial t} = D \frac{\partial^2 C}{\partial x_j \partial x_j} - \frac{\partial}{\partial x_i}\left(u_{pi} C\right) \tag{2}$$

where *D* is the coefficient of diffusion and u_{pi} is the particle velocity in the direction *i*. The particle velocity can be considered with some simplification as (see also [4])

$$u_{pi} \approx u_i + u_{si} \tag{3}$$

where u_i is the *i*-th component of the fluid velocity, u_{si} is the *i*-th component of the settling velocity of particles. When the particles are assumed to be spherical and sufficiently small the settling velocity can be expressed using Stoke's settling velocity law as

$$u_{si} = \frac{d^2(\rho_p - \rho)}{18 \mu f} g_i \tag{4}$$

Here, *d* is the particle diameter, ρ_p is the particle density, *f* is the correction for non-Stokesian drag and g_i is the gravity vector component $\mathbf{g} = \{0, -g\}$ [1].

Equations (1) and (2) can be made dimensionless using transformations of coordinates and velocities

$$\tilde{x_i} = \frac{x_i}{L} \qquad \tilde{u}_i = \frac{u_i}{u_b} \tag{5}$$

where *L* is the characteristic length and u_b is the bulk velocity defined as [2]

$$u_b = \sqrt{\tilde{g} L} \qquad \tilde{g} = g \frac{\rho_1 - \rho_0}{\rho_0} \tag{6}$$

The dimensionless concentration and pressure can be defined as

$$\tilde{C} = \frac{\rho - \rho_0}{\rho_1 - \rho_0} \qquad \tilde{p} = \frac{p}{\rho_0 u_b^2} \tag{7}$$

The dimensionless governing equations can be written as

$$\begin{aligned} \frac{\partial \tilde{u}_i}{\partial x_i} &= 0 \\ \frac{\partial \tilde{u}_i}{\partial t} + \frac{\partial}{\partial x_j}\left(\tilde{u}_j \tilde{u}_i\right) &= -\frac{\partial \tilde{p}}{\partial x_i} + \frac{1}{\sqrt{Gr}} \frac{\partial^2 \tilde{u}_i}{\partial x_j \partial x_j} - \tilde{C} e_i^g \\ \frac{\partial \tilde{C}}{\partial t} &= \frac{1}{Sc\sqrt{Gr}} \frac{\partial^2 \tilde{C}}{\partial x_j \partial x_j} - \frac{\partial}{\partial x_i}\left(\tilde{u}_{pi} \tilde{C}\right) \end{aligned} \tag{8}$$

where $e_i^g = (0, -1)$ is the unity vector pointing in the direction of gravity. Three dimensionless parameters appear in (8), namely the Grashof number *Gr*, the Schmidt number *Sc*, and the dimensionless particle velocity $\tilde{u}_{pi}$ which are defined as [3]

$$Gr = \left(\frac{u_b L}{\nu}\right)^2 \qquad Sc = \frac{\nu}{D} \qquad \tilde{u}_{pi} = \tilde{u}_i + \tilde{u}_{si} \tag{9}$$

Using a characteristic-based split (CBS) algorithm we get the following system of equations (details see e.g. in [5] [6])

$$\begin{aligned} \tilde{u}_i^* = \tilde{u}_i^n + \Delta t \Bigg[& \frac{1}{\sqrt{Gr}} \frac{\partial^2 \tilde{u}_i}{\partial x_j \partial x_j} - \tilde{C} e_i^g - \frac{\partial}{\partial x_j}\left(\tilde{u}_j \tilde{u}_i\right) + \\ & \frac{\Delta t}{2} \tilde{u}_k \frac{\partial}{\partial x_k}\left(\frac{\partial}{\partial x_j}\left(\tilde{u}_j \tilde{u}_i\right) + \tilde{C} e_i^g\right) \Bigg]^n \end{aligned} \tag{10}$$

$$\tilde{u}_i^{n+1} = \tilde{u}_i^* - \Delta t \frac{\partial \tilde{p}^{n+1}}{\partial x_i} \tag{11}$$

$$\frac{\partial^2 \tilde{p}^{n+1}}{\partial x_i \partial x_i} = \frac{1}{\Delta t} \frac{\partial \tilde{u}_i^*}{\partial x_i} \tag{12}$$

where we used the intermediate velocity $\tilde{u}_i^*$ which does not satisfied a continuity equation in (8). Upper indexes *n* and *n+1* indicate time steps and $\Delta t = t^{n+1} - t^n$ is the length of the time interval.

In the last step the dimensionless concentration $\tilde{C}$ can be also solved using the CBS algorithm (see [6])

$$\begin{aligned} \tilde{C}^{n+1} = \tilde{C}_i^n + \Delta t \Bigg[& \frac{1}{Sc\sqrt{Gr}} \frac{\partial^2 \tilde{C}^n}{\partial x_j \partial x_j} - \frac{\partial}{\partial x_j}\left(\tilde{u}_{pj}^{n+1} \tilde{C}^n\right) + \\ & \frac{\Delta t}{2} \tilde{u}_{pk}^{n+1} \frac{\partial}{\partial x_k}\left(\frac{\partial}{\partial x_j}\left(\tilde{u}_{pj}^{n+1} \tilde{C}^n\right)\right) \Bigg] \end{aligned} \tag{13}$$

3 LOCAL BOUNDARY INTEGRAL FORMULATION

The area of interest Ω with the boundary Γ is covered by points within the area and also on the global boundary (see Fig. 1). Consider a local circular sub-domain Ω_s with boundary Λ_s centered at every point *s*. This sub-domain is regular around all of the internal points, but at the points on the global boundary this local boundary consists of a part of the global boundary intersected with the local sub-domain Γ_s (see Fig. 2). To express the local boundary integral form of the governing equations developed in the previous section in a domain Ω_s, we apply the weighting residual principle [7] to equations (10), (11), (12), and (13) to obtain the weak form. If the test function w^* is chosen to be the fundamental solution of the Laplace equation, then after integration by parts twice the following integral equations can be obtained (see also [8])

$$\begin{aligned}\int_{\Omega_s} \tilde{u}_i^* w^* d\Omega = \int_{\Omega_s} \tilde{u}_i^n w^* d\Omega - \Delta t \Bigg[\int_{\Omega_s} \tilde{u}_j \frac{\partial \tilde{u}_i}{\partial x_j} w^* d\Omega + \int_{\Omega_s} \tilde{C} e_i^g w^* d\Omega \\ + \frac{1}{\sqrt{Gr}} \left(c_s \tilde{u}_{is} + \int_{\Lambda_s \cup \Gamma_s} \frac{\partial w^*}{\partial n} \tilde{u}_i d\Gamma - \int_{\Lambda_s \cup \Gamma_s} w^* \frac{\partial \tilde{u}_i}{\partial n} d\Gamma \right) \\ - \frac{\Delta t}{2} \int_{\Omega_s} \tilde{u}_k \frac{\partial}{\partial x_k} \left(\tilde{u}_j \frac{\partial \tilde{u}_i}{\partial x_j} + \tilde{C} e_i^g \right) w^* d\Omega \Bigg]^n \end{aligned} \tag{14}$$

$$c_s \tilde{p}_s^{n+1} + \int_{\Lambda_s \cup \Gamma_s} \frac{\partial w^*}{\partial n} \tilde{p}^{n+1} d\Gamma - \int_{\Lambda_s \cup \Gamma_s} w^* \frac{\partial \tilde{p}^{n+1}}{\partial n} d\Gamma + \frac{1}{\Delta t} \int_{\Omega_s} \frac{\partial \tilde{u}_i^*}{\partial x_i} w^* d\Omega = 0. \tag{15}$$

$$\begin{aligned}\int_{\Omega_s} \tilde{C}^{n+1} w^* d\Omega = \int_{\Omega_s} \tilde{C}^n w^* d\Omega - \Delta t \Bigg[\int_{\Omega_s} \tilde{u}_j^{n+1} \frac{\partial \tilde{C}^n}{\partial x_j} w^* d\Omega \\ + \frac{1}{Sc\sqrt{Gr}} \left(c_s \tilde{C}_s^n + \int_{\Lambda_s \cup \Gamma_s} \frac{\partial w^*}{\partial n} \tilde{C}^n d\Gamma - \int_{\Lambda_s \cup \Gamma_s} w^* \frac{\partial \tilde{C}^n}{\partial n} d\Gamma \right) \\ - \frac{\Delta t}{2} \int_{\Omega_s} \tilde{u}_k^{n+1} \frac{\partial}{\partial x_k} \left(\tilde{u}_j \frac{\partial \tilde{C}^n}{\partial x_j} \right) w^* d\Omega \Bigg] \end{aligned} \tag{16}$$

Here the coefficient c_s is equal to 1 for interior points and equal to $\frac{\theta}{2\pi}$ for points on the global boundary (see Fig. 2).

The boundary $\Lambda_s \cup \Gamma_s$ is then divided into several boundary elements (see Fig. 2). The values of velocity, pressure, and concentration in node *s* can now be computed from values in the local elements. The pressure equation (15) now becomes

$$c_s \tilde{p}_s + \int_{\Lambda_s \cup \Gamma_s} \frac{\partial w_{sj}^*}{\partial n} \tilde{p}_j d\Gamma - \int_{\Lambda_s \cup \Gamma_s} w_{sj}^* \frac{\partial \tilde{p}_j}{\partial n} d\Gamma - \int_{\Omega_s} w_{sj}^* \frac{\partial \tilde{u}_i^*}{\partial x_i} d\Omega = 0. \tag{17}$$

To avoid the term $\frac{\partial \tilde{p}_j}{\partial n}$ defined on the local boundary Λ_s, we use a companion solution (see e. g. [9]). This solution satisfies the Laplace equation and is equal to the fundamental solution on the local boundary. For the 2D Laplace equation the companion solution is defined as

$$w^c = \frac{1}{2\pi} log \left(\frac{1}{r_0} \right), \tag{18}$$

where r_0 is the radius of the local domain Ω_s. Equation (17) becomes

$$c_s \tilde{p}_s + \int_{\Lambda_s \cup \Gamma_s} \frac{\partial w_{sj}^*}{\partial n} \tilde{p}_j d\Gamma - \int_{\Gamma_s} \left(w_{sj}^* - w_{sj}^c \right) \frac{\partial \tilde{p}_j}{\partial n} d\Gamma - \int_{\Omega_s} \left(w_{sj}^* - w_{sj}^c \right) \frac{\partial \tilde{u}_i^*}{\partial x_i} d\Omega = 0. \tag{19}$$

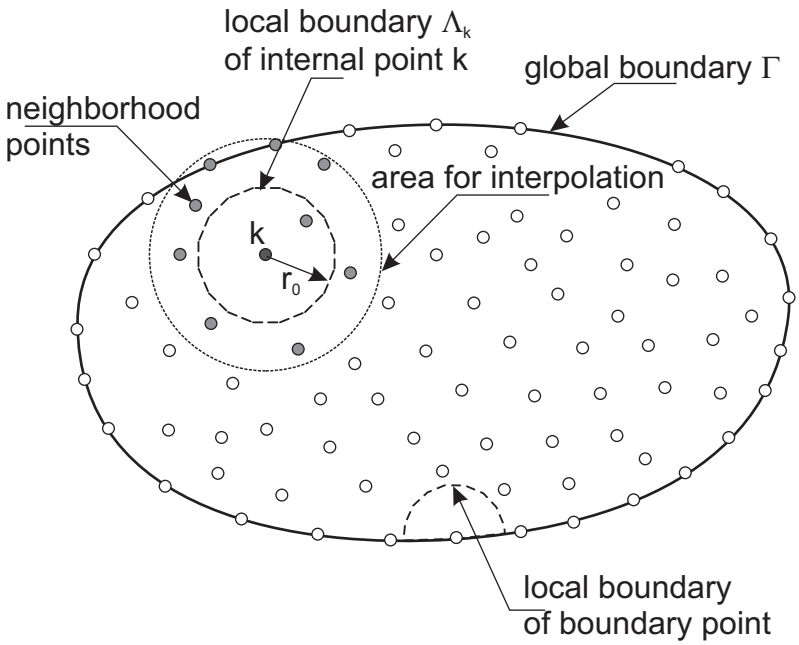

Figure 1: Points in the global area

Unknown values of the pressure and its derivatives in the local boundary element *j* can now be approximated by values of the pressure in *N* neighbouring points using RBF interpolation. The main reason for using RBF instead of the moving least squares (MLS) interpolation is that RBFs possess the delta property, making the prescription of the boundary conditions straightforward and simple. Multiquadric RBFs are used here

$$W(r_{ij}) = \sqrt{r_{ij}^2 + R^2} \tag{20}$$

where $W(r_{ij})$ is the multiquadric RBF between points *i* and *j* (see [10], [7]), r_{ij} is the Euclidean distance between these two points and *R* is the so-called shape factor of the multiquadric function. The formula of Hardy with a slight modification is applied to the local RBFs (see [10]) to find the optimal value of the shape factor, which can be computed in point *i* as

$$R_i = \frac{0.815}{N} \sum_{j=1}^{N} d_j \tag{21}$$

where d_j is the distance between the j-th local supporting point and its closest neighbouring point. A technique described in detail in [7] can be used to obtain a set of RBF shape functions Φ_{ij}, which can be used to express the pressure and its derivatives in the point *i* as

$$\tilde{p}_i = \sum_{j=1}^{N} \Phi_{ij} \tilde{p}_j \quad \frac{\partial \tilde{p}_i}{\partial x_k} = \sum_{j=1}^{N} \frac{\partial \Phi_{ij}}{\partial x_k} \tilde{p}_j \tag{22}$$

Using these shape functions causes equation (19) to become

$$c_s \tilde{p}_s + \sum_{m=1}^{N} \left(\int_{\Lambda_s \cup \Gamma_s} \frac{\partial w_{sj}^*}{\partial n} \Phi_{jm} d\Gamma \right) \tilde{p}_m - \sum_{m=1}^{N} \left[\int_{\Gamma_s} \left(w_{sj}^* - w_{sj}^c \right) \frac{\partial \Phi_{jm}}{\partial n} d\Gamma \right] \tilde{p}_m - \tag{23}$$
$$- \sum_{m=1}^{N} \left[\int_{\Omega_s} \left(w_{sj}^* - w_{sj}^c \right) \frac{\partial \Phi_{jm}}{\partial x_i} d\Omega \right] \tilde{u}_{im}^* = 0,$$

A similar procedure can be applied to equations (14) and (16). All of these equations can then be formulated in matrix form as

$$\sum_{m=1}^{N} M_{sm}\tilde{u}_{im}^{*} = \sum_{m=1}^{N} M_{sm}\tilde{u}_{im}^{n} - \Delta t \left[\sum_{m=1}^{N} S_{sm}\tilde{u}_{im} + e_i^g \sum_{m=1}^{N} M_{sm}\tilde{C}_m + \right. \tag{24}$$
$$+ \frac{1}{\sqrt{Gr}} \left(c_s \tilde{u}_{is} + \sum_{m=1}^{N} H_{sm}\tilde{u}_{im} - \sum_{m=1}^{N} G_{sm}\tilde{u}_{im} \right) -$$
$$\left. - \frac{\Delta t}{2} \sum_{m=1}^{N} \left(U_{sm}\tilde{u}_{im} + e_i^g F_{sm}\tilde{C}_m \right) \right]^n,$$

$$\sum_{m=1}^{N} M_{sm}\tilde{u}_{im}^{n+1} = \sum_{m=1}^{N} M_{sm}\tilde{u}_{im}^{*} - \Delta t \sum_{m=1}^{N} S_{sm}\tilde{p}_m \tag{25}$$

$$c_s\tilde{p}_s + \sum_{m=1}^{N} H_{sm}\tilde{p}_m - \sum_{m=1}^{N} G_{sm}\tilde{p}_m - \sum_{m=1}^{N} S_{sm}\tilde{u}_{im}^{*} = 0, \tag{26}$$

$$\sum_{m=1}^{N} M_{sm}\tilde{C}_m^{n+1} = \sum_{m=1}^{N} M_{sm}\tilde{C}_m^{n} - \Delta t \left[\sum_{m=1}^{N} S_{sm}\tilde{C}_m + \right. \tag{27}$$
$$\left. + \frac{1}{Sc\sqrt{Gr}} \left(c_s\tilde{C}_s + \sum_{m=1}^{N} H_{sm}\tilde{C}_m - \sum_{m=1}^{N} G_{sm}\tilde{C}_m \right) - \frac{\Delta t}{2} \sum_{m=1}^{N} U_{sm}\tilde{C}_m \right]^n,$$

where $\tilde{u}_{im}$, $\tilde{p}_m$, and $\tilde{C}_m$ are the values of the dimensionless velocity, pressure and concentration, respectively, in the points neighbouring the reference point *s*. The matrices M_{sm}, H_{sm}, G_{sm}, S_{sm}, and U_{sm} can be written as

$$M_{sm} = \sum_{j=1}^{n_e} \int_{\Omega_{sj}} \left(w_{sj}^{*} - w_{sj}^{c} \right) \Phi_{jm} d\Omega, \tag{28}$$

$$H_{sm} = \sum_{j=1}^{n_e} \int_{\Lambda_{sj} \cup \Gamma_{sj}} \frac{\partial w_{sj}^{*}}{\partial n} \Phi_{jm} d\Gamma,$$

$$G_{sm} = \sum_{j=1}^{n_e} \int_{\Gamma_{sj}} \left(w_{sj}^{*} - w_{sj}^{c} \right) \frac{\partial \Phi_{jm}}{\partial n} d\Gamma,$$

$$S_{sm} = \tilde{u}_{km} \sum_{j=1}^{n_e} \int_{\Omega_{sj}} \left(w_{sj}^{*} - w_{sj}^{c} \right) \frac{\partial \Phi_{jm}}{\partial x_k} d\Omega,$$

$$U_{sm} = \sum_{j=1}^{n_e} \int_{\Omega_{sj}} \frac{\partial \left(w_{sj}^{*} u_{im} \right)}{\partial x_i} \frac{\partial \left(u_{im} \Phi_{jm} \right)}{\partial x_i} d\Omega,$$

$$F_{sm} = \sum_{j=1}^{n_e} \int_{\Omega_{sj}} \frac{\partial \left(w_{sj}^{*} u_{im} \right)}{\partial x_i} \Phi_{jm} d\Omega$$

where n_e is the number of local elements, Λ_{sj} is the j-th internal local boundary element, Γ_{sj} is the j-th local boundary element situated on the intersection of the global boundary, and Ω_{sj} is the triangular area element (see Fig. 2). The mass matrix M_{sm} can be used in either a full or a lumped form. The lumped form is used here, because it eliminates a matrix inversion procedure.

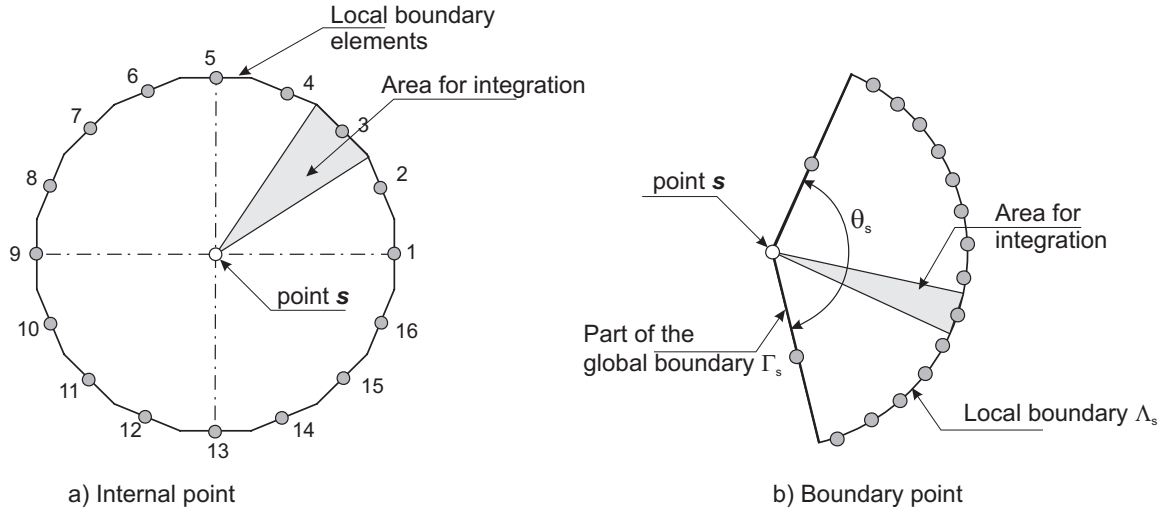

Figure 2: Local network around point

4 NUMERICAL EXAMPLES

All examples present so-called lock-exchange flow in rectangular channel when two fluids of different densities are divided by a vertical barrier at the initial time $t_0 = 0$. When this barrier is removed the denser liquid intrudes into the light one. This type of current is also frequently studied experimentally.

The schemes and boundary conditions of all these examples are presented in Fig.3.

4.1 Flow without any obstacles

The first example has a smooth bed without any obstacles and it serves as a comparing one. The rectangular computational domain of size $L = 20 \times H = 2$ is covered by the uniform grid of 800×80 points. The Grashof number $Gr = 5 \times 10^6$ is used for simulation, the Schmidt number is Sc=1 and the dimensionless settling velocity of particles is $\tilde{u}_s = 0.02$. Fig. 4 presents the results of the particle current at five dimensionless time instances. The flow is characterized by contours of particle concentration. Soon after beginning an intrusion, a front forms in the shape of a lifted nose due to the no-slip boundary condition on the bottom bed of the channel and Kelvin-Helmholtz vortices are formed at the upper part of the current.

4.2 Flow through the low obstacle

The second example presents the flow of particle current over a low rectangular obstacle (see Fig.3b). The dimensionless height of the obstacle is $d = 0.5$, i. e. $H/d = 4$. This obstacle is located in the dimensionless distance $L_s = 4.0$ from the beginning of a channel. The parameters of this example remain the same as in the first one. Fig. 5 presents contours of the particle concentration. Approximately at time $\tilde{t} = 6$ the current hits the upstream part of the obstacle and some deformation of the current starts. The whole current is divided into parts during the next time steps. The first part forms the backward current which moves back to the left part of the channel; the second part overcome the obstacle and continues moving in the right part of the channel.

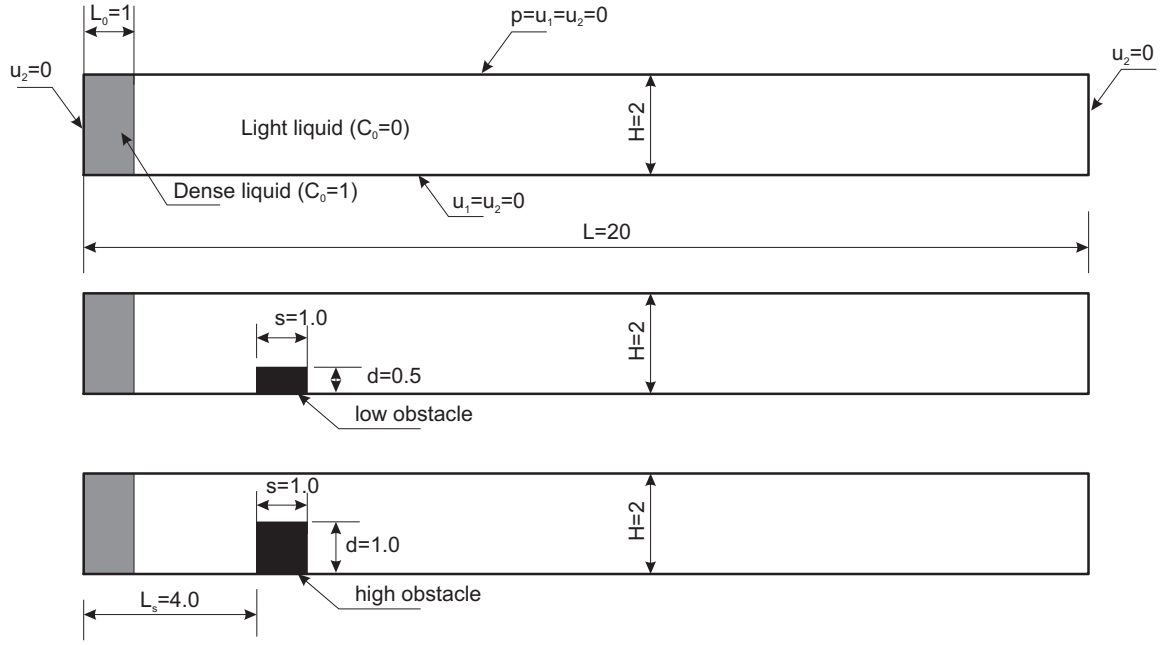

Figure 3: Numerical examples, geometry and boundary conditions

4.3 Flow through the high obstacle

The third example presents the flow over a high rectangular obstacle (see Fig.3c). The dimensionless height of the obstacle is now $d = 1.0$, i. e. $H/d = 2$. The location of the obstacle and parameters of flow remain the same as in the previous example. Fig. 6 presents contours of concentration. As can be seen in Fig.6 the deformation of the particle current is now a bit different than in the previous example. Almost all particles form now the backward wave and only the negligible amount of particles overcome the obstacle. The newly formed backward current is now more accentuated.

The shear stress distribution at the bottom of the channel is a very important part of the resuspension of particles. The dimensionless shear stress $\tilde{\tau}_w$ can be described as [1, 3, 6]

$$\tilde{\tau}_w = \frac{1}{\sqrt{Gr}} \sqrt{\left(\frac{\partial u_{p1}}{\partial x_2}\right)^2 + \left(\frac{\partial u_{p2}}{\partial x_2}\right)^2} \tag{29}$$

Fig. 7 presents the dimensionless shear stress at the bottom boundary at time intervals $\tilde{t}$ =4, 6, and 10. This shear stress shows several peaks that correspond to the front of the current and also to the Kelvin-Helmholtz vortices. The low values of the shear stress reflect mentioned decay of current in the case of low and high obstacles at time $\tilde{t} = 10$ (see Fig.7b,c).

The cumulative sedimentation of particles can be computed as (see [1])

$$D(\tilde{x}, \tilde{t}) = \frac{1}{L_0 H} \int_0^{\tilde{t}} \tilde{C}_w(\tilde{x}, \hat{t}) u_s d\hat{t} \tag{30}$$

Fig. 8 shows the value of this deposit as a function of the longitudinal coordinate x at the dimensionless time $\tilde{t}$=60. The cumulative sedimentation is concentrated in the upstream part of the channel in case of low and especially high obstacles.

Fig. 9 presents temporal variations of the mean dimensionless pressure $\tilde{p}$ (7) acting on the upstream and downstream faces of the obstacles. The maximum impact is localized at time $\tilde{t} = 6$.

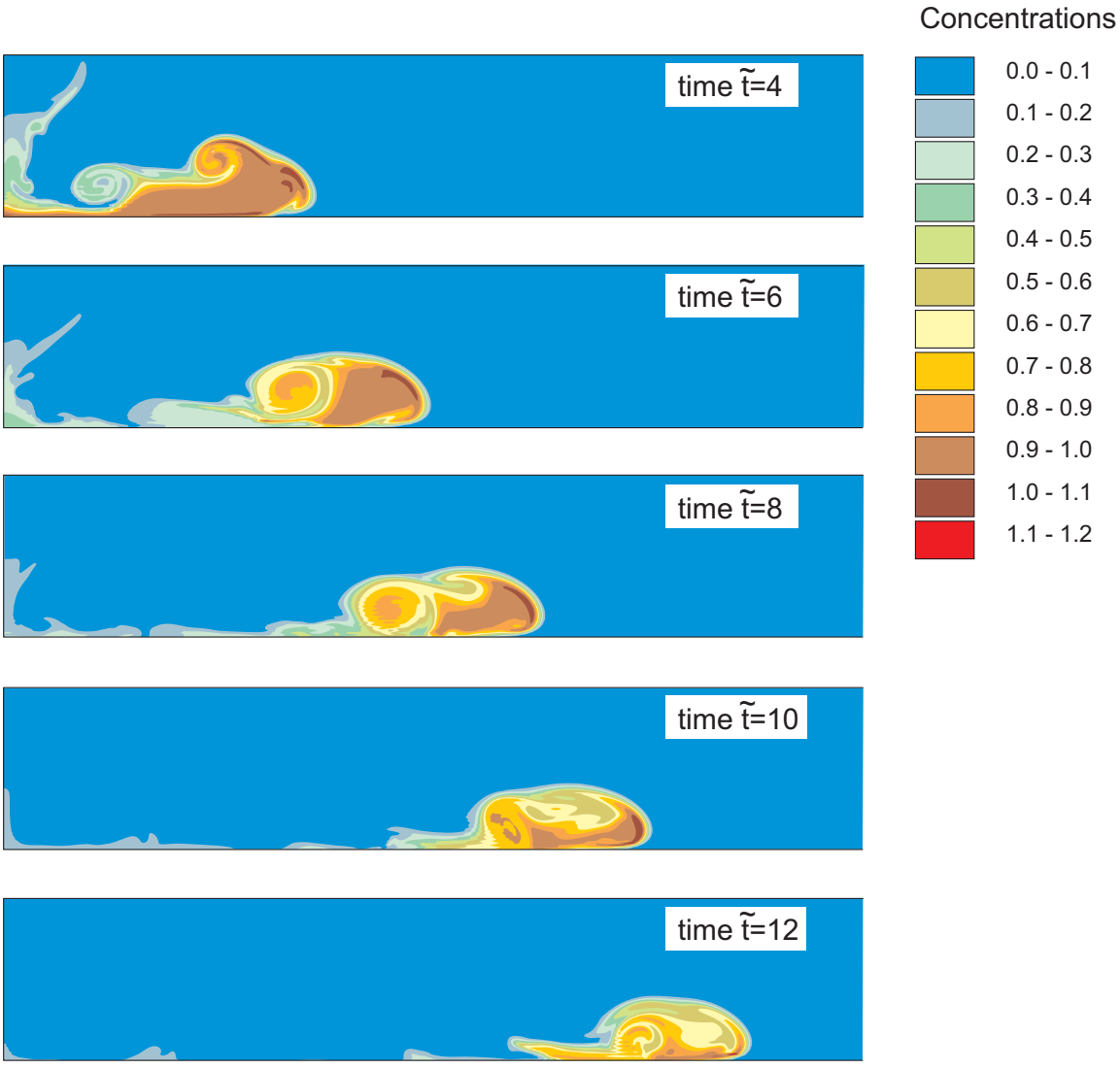

Figure 4: Dimensionless concentrations in the channel without any obstacles

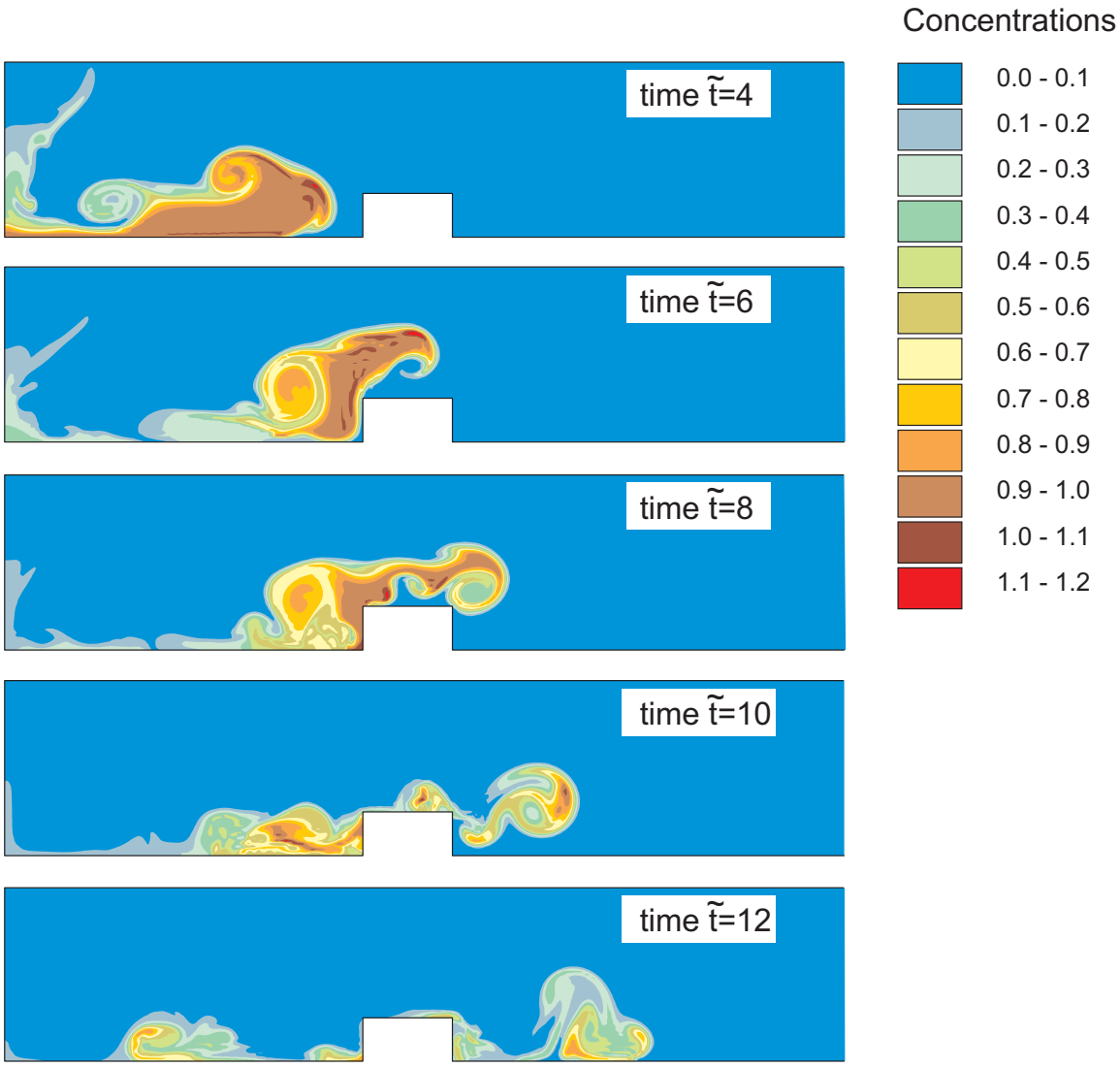

Figure 5: Dimensionless concentrations in the channel with the low obstacle

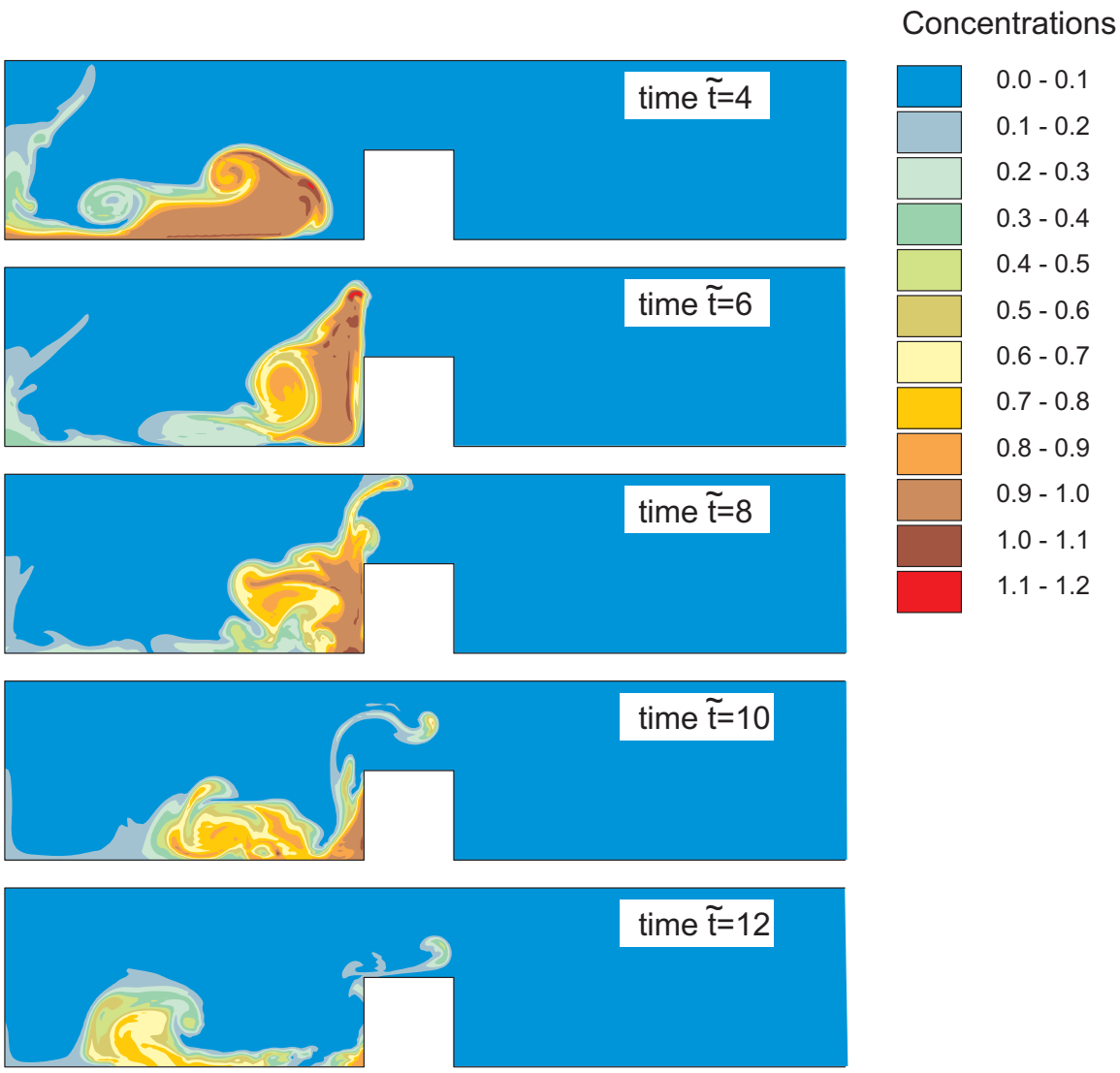

Figure 6: Dimensionless concentrations in the channel with the low obstacle

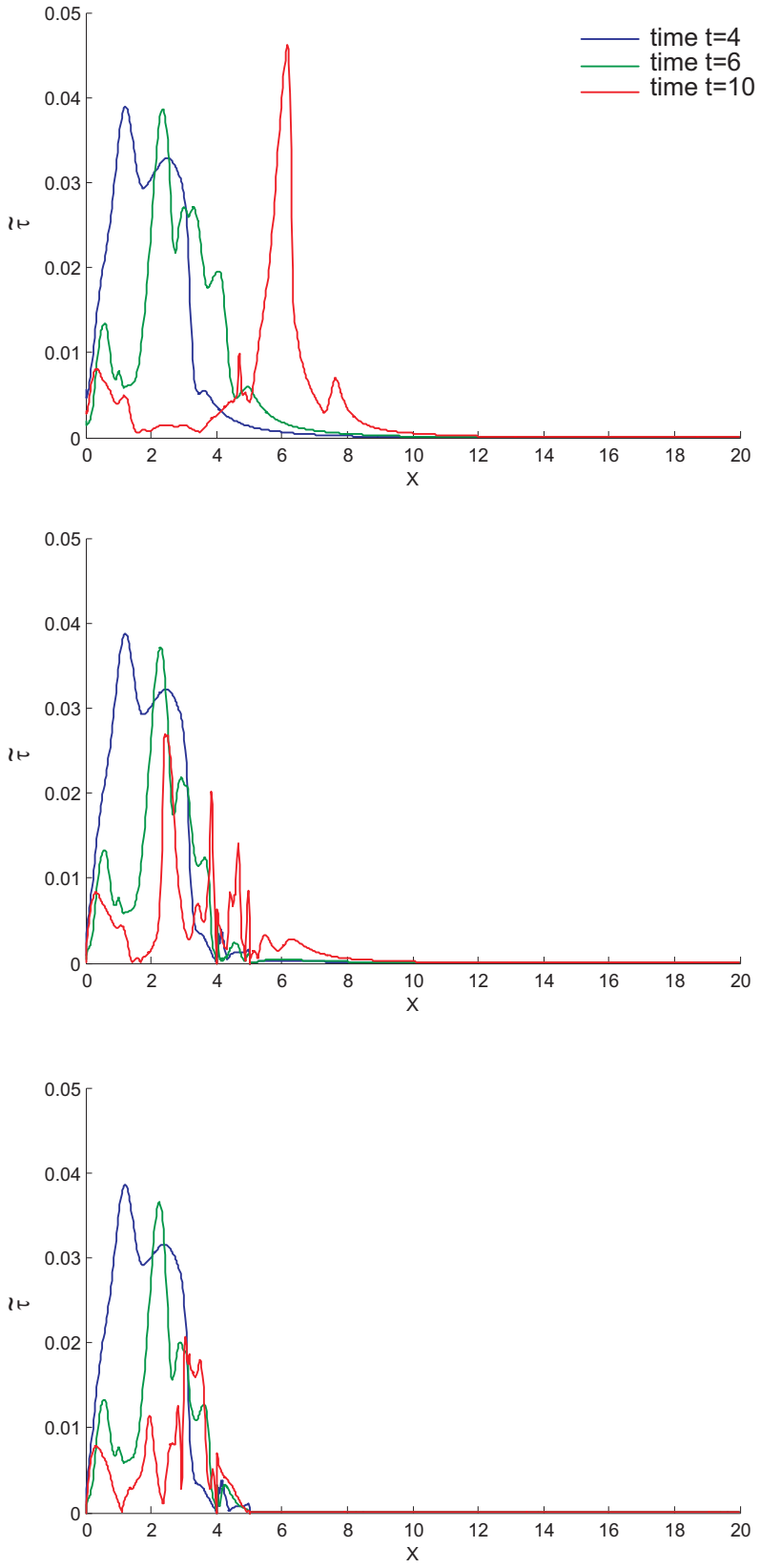

Figure 7: Dimensionless bed shear stress; a–without obstacle, b–low obstacle, c–high obstacle

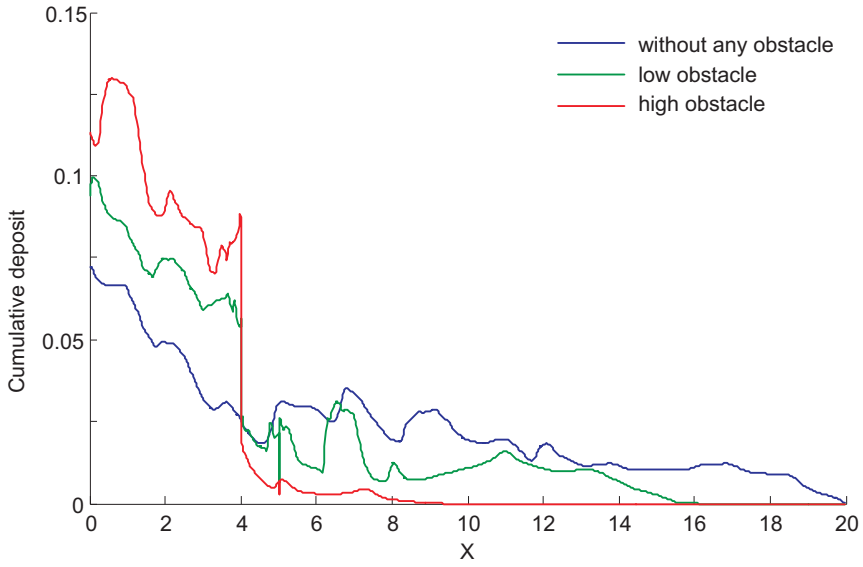

Figure 8: Dimensionless cumulative particle deposit at time $\tilde{t}$=60; a–without obstacle, b–low obstacle, c–high obstacle

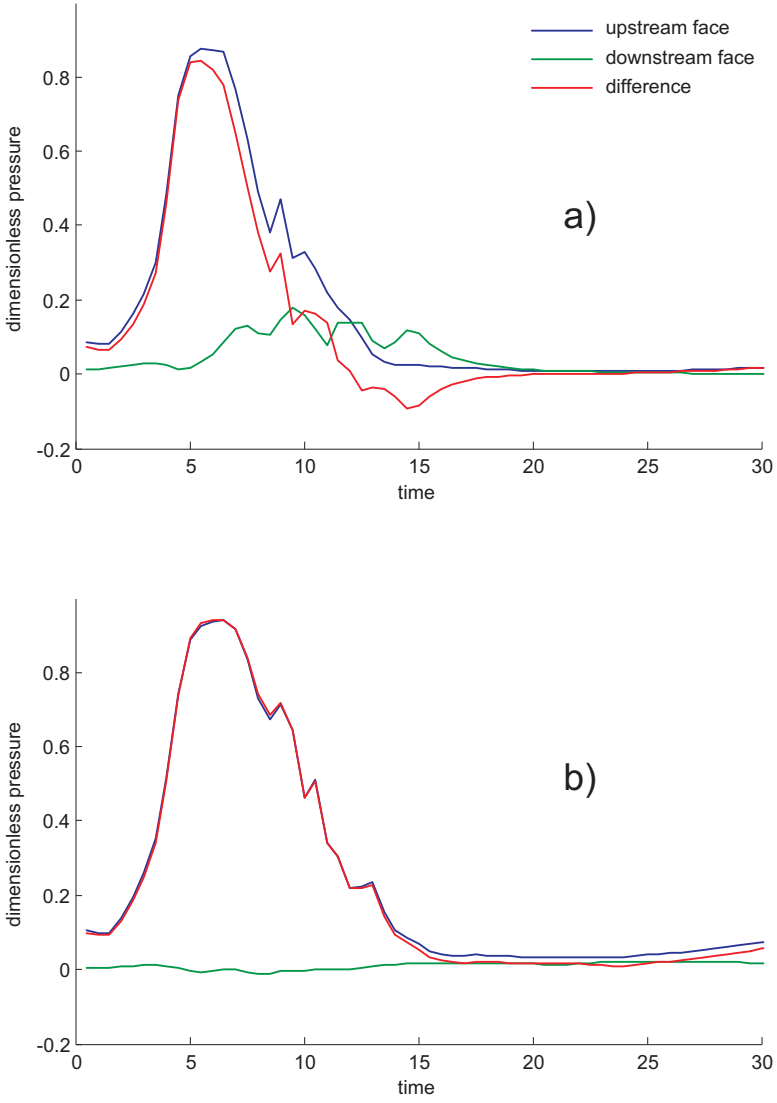

Figure 9: Drag acting on the obstacles; a–low obstacle, b–high obstacle

5 CONCLUSIONS

This paper presents a possible use of the LBIEM meshless method for solution of the gravity currents flow. We use the characteristic based split scheme to achieve stable and accurate results. The results obtained from test cases proved that the method is an effective and useful tool to solve this type of flow and can be used as an effective tool for modelling of several types of geohazards.

ACKNOWLEDGEMENT

This contribution was supported by PARAGEO project, co-funded by the EEA Grants and the state budget of the Slovak Republic from the EEA Scholarship Program Slovakia under the contract EHP-30/SK06-IV-02-007/2015.

REFERENCES

[1] M. I. Cantero, S. Balachandar, M. H. Garcia, An EulerianEulerian model for gravity currents driven by inertial particles, *International Journal of Multiphase Flow*, **34**, 484-501, 2008.

[2] C. Härtel, E. Meiburg, F. Necker, Analysis and direct numerical simulation of the flow at a gravity-current head. Part 1. Flow topology and front speed for slip and no-slip boundaries. *Journal of Fluid Mechanics*, **418**, 189-212, 2000.

[3] F. Necker, C. Härtel, L. Kleiser, E. Meiburg, High-resolution simulations of particle-driven gravity currents, *International Journal of Multiphase Flow* **28** 279–300, 2002.

[4] L. Espath, L. Pinto, S. Laizet, J. Silvestrini, Two- and three-dimensional Direct Numerical Simulation of particle-laden gravity currents, *Computers & Geosciences* **63** 9–16, 2014.

[5] K. Kovářík, J. Mužík, D. Sitányiová, A fractional step local boundary integral element method for unsteady two-dimensional incompressible flow, *Engineering Analysis with Boundary Elements* **44** 55–63, 2014.

[6] K. Kovářík, J. Mužík, S. Masarovičová, D. Sitányiová, A local boundary integral method for two-dimensional particle-driven gravity currents simulation, *Engineering Analysis with Boundary Elements* **56** 119–128, 2015.

[7] K. Kovářík, J. Mužík, M. S. Mahmood, A meshless solution of two dimensional unsteady flow, *Engineering Analysis with Boundary Elements* **36** 738–743, 2012.

[8] S. N. Atluri, H.-G. Kim, J. Y. Cho, A critical assessment of the truly Meshless Local Petrov-Galerkin (MLPG), and Local Boundary Integral Equation (LBIE) methods, *Computational Mechanics* **24** 348–372, 1999.

[9] V. Sladek, J. Sladek, S. N. Atluri, R. Van Keer, Numerical integration of singularities in meshless implementation of local boundary integral equations, *Computational Mechanics* **25** 394–403, 2000.

[10] E. J. Sellountos, A. Sequeira, An advanced meshless LBIE/RBF method for solving two-dimensional incompressible fluid flows, *Computational Mechanics* **41** (2007) 617–631.